J. Fluid Mech. (2015), *vol.* 768, *pp.* 113–140.
doi:10.1017/jfm.2015.72

Linear three-dimensional global and asymptotic stability analysis of incompressible open cavity flow

Vincenzo Citro[1,†], Flavio Giannetti[1], Luca Brandt[2] and Paolo Luchini[1]

[1]DIIN, University of Salerno, Via Giovanni Paolo II, 84084 Fisciano (SA), Italy

[2]Linné Flow Centre and SeRC (Swedish e-Science Research Centre), KTH Mechanics, S-100 44 Stockholm, Sweden

(Received 21 May 2014; revised 19 December 2014; accepted 1 February 2015; first published online 4 March 2015)

The viscous and inviscid linear stability of the incompressible flow past a square open cavity is studied numerically. The analysis shows that the flow first undergoes a steady three-dimensional bifurcation at a critical Reynolds number of 1370. The critical mode is localized inside the cavity and has a flat roll structure with a spanwise wavelength of about 0.47 cavity depths. The adjoint global mode reveals that the instability is most efficiently triggered in the thin region close to the upstream tip of the cavity. The structural sensitivity analysis identifies the wavemaker as the region located inside the cavity and spatially concentrated around a closed orbit. As the flow outside the cavity plays no role in the generation mechanisms leading to the bifurcation, we confirm that an appropriate parameter to describe the critical conditions in open cavity flows is the Reynolds number based on the average velocity between the two upper edges. Stabilization is achieved by a decrease of the total momentum inside the shear layer that drives the core vortex within the cavity. The mechanism of instability is then studied by means of a short-wavelength approximation considering pressureless inviscid modes. The closed streamline related to the maximum inviscid growth rate is found to be the same as that around which the global wavemaker is concentrated. The structural sensitivity field based on direct and adjoint eigenmodes, computed at a Reynolds number far higher than that of the base flow, can predict the critical orbit on which the main instabilities inside the cavity arise. Further, we show that the sub-leading unstable time-dependent modes emerging at supercritical conditions are characterized by a period that is a multiple of the revolution time of Lagrangian particles along the orbit of maximum growth rate. The eigenfrequencies of these modes, computed by global stability analysis, are in very good agreement with the asymptotic results.

Key words: bifurcation, instability, separated flows

1. Introduction

Flow separation and recirculation are of great interest as they play an important role in the phenomena involved in transport and mixing processes. The flow past open

† Email address for correspondence: vcitro@unisa.it

cavities is a prototype of geometrical configurations characterized by a finite region of separated flow. The identification of the flow characteristics related to instability mechanisms (e.g. coherent structures) is also of practical importance since these may lead to resonances, acoustic noise or structural vibrations. Rockwell & Naudascher (1978) classified the unstable behaviour of this kind of flow into fluid-dynamic, fluid-resonant, and fluid-elastic.

Acoustic resonance (i.e. fluid-resonant behaviour) has received a remarkable amount of attention in the past due its relation with the noise generation process (Rossiter 1964; Yamouni, Sipp & Jacquin 2013). In this case, there exists a feedback mechanism between the unstable shear layer susceptible to Kelvin–Helmholtz instability and the pressure waves (Rowley, Colonius & Basu 2002). Gharib & Roshko (1987) observed experimentally that the increase of the cavity length to depth ratio (L/D) led to a different kind of instability, the so-called 'wake mode'. This global instability relies on a purely hydrodynamic mechanism (the oscillation Strouhal number is weakly dependent on the Mach number) and is characterized by a large-scale vortex shedding.

1.1. *Experimental and numerical investigations of three-dimensional instabilities*

Three-dimensional structures in cavities with large span-to-chord ratios were first reported by Maull & East (1963) using oil flow and static-pressure measurements. These authors observed stable cell formations inside open rectangular cavities of different aspect ratios (L/D). Rockwell & Knisely (1980) observed a strong coupling between the growth of the primary vortices and the increase of the vorticity of the longitudinal vortices past the downstream edge of the cavity. They concluded that, because of this interaction, the cavity core vortex presents an ordered spanwise modulation. These coherent structures were analysed in detail in the laminar regime by Faure *et al.* (2007, 2009) in cavities with an aspect ratio varying between 0.5 and 2. Using smoke visualizations, Faure *et al.* (2007) report mushroom-like counter-rotating vortical structures and suggest that the resulting inherent flow is the consequence of a centrifugal instability related to the cavity core vortex.

Brés & Colonius (2007*b*) performed numerical simulations of the linearized compressible Navier–Stokes equations to investigate the instability features in open cavity flows. These authors identify the onset of the first bifurcation over a wide range of Mach numbers and cavity aspect ratios and discuss the variations of the spanwise modulation with the cavity depth. Brés & Colonius (2007*a*) showed, furthermore, that the full nonlinear results, computed by direct numerical simulation (DNS), agree very well with the features of the three-dimensional global mode provided by linear stability analysis. Brés & Colonius (2008) accurately discuss the properties, the structure and the nature of such instability. Using the generalized Rayleigh criterion (Bayly 1988), they show that the instability is a centrifugal instability associated with the closed streamlines inside the cavity.

Faure *et al.* (2009) performed an experimental investigation aimed at understanding the three-dimensional flow topology inside cavities of different shapes and for several Reynolds numbers. These authors also performed a secondary instabilities analysis and identified the relevant shear-layer and inner-cavity flow scales. Zhang & Naguib (2006, 2008, 2011) carried out a systematic study of the effect of the sidewalls on the unsteady open cavity flow at low Mach number. The presence of the sidewalls is shown to lead to strong amplifications of the pressure fluctuations inside the cavity. Lasagna *et al.* (2011) investigated the effects of a trapped vortex cell (TVC) on the

aerodynamic performance of a wing model and found a three-dimensional organization of the flow inside the cell according to the value of the angle of attack and the Reynolds number. di Cicca *et al.* (2013) reported time-resolved tomographic particle image velocimetry (PIV) measurements in rectangular cavities having the length-to-depth ratio equal to 2, 3 and 4.

Very recently, de Vicente *et al.* (2014) examined both experimentally and numerically the instabilities over a rectangular open cavity of aspect ratio $L/D = 2$. These authors compared the linear three-dimensional instability results with the spatial structure of the experimental fields, showing qualitative agreement for the main flow characteristics. Furthermore, they also show that modifications of the spanwise boundary conditions can cause significant alterations of the flow field due to nonlinear effects. Finally, Meseguer-Garrido *et al.* (2014) present a systematic study of the onset of the first instability, varying the Reynolds number, the incoming boundary-layer thickness and the cavity aspect ratio.

Experimental studies on the formation of three-dimensional structures in the start-up flow inside a lid-driven cavity (LDC) can be found in Migeon, Texier & Pineau (2000), Guermond *et al.* (2002) and Migeon, Pineau & Texier (2003). These three-dimensional modulations inside the cavities are also documented by de Vicente *et al.* (2010) and Gonzalez *et al.* (2011) who considered complex cross-sectional shapes.

1.2. *Short-wave asymptotic analysis*

Instabilities in open and closed cavities, as well as in separated flows, are interpreted as centrifugal instabilities. Centrifugal short-wave instabilities were first considered by Bayly (1988) who used the geometrical optics approximation and Flouquet theory to extend the classical Rayleigh theory for centrifugal instabilities to general inviscid planar flows. Bayly proposed diagonalizing the convective operator of the linearized Euler equations (LEes) and constructing linear asymptotic eigenmodes in the limit of large spanwise wavenumber using a Wentzel–Kramers–Brillouin–Jeffreys (WKBJ) expansion, localized on the closed orbit characterized by the maximum Floquet exponent. Later, the same author showed qualitative agreement between the results obtained with the linearized Navier–Stokes equations and the asymptotic predictions (Bayly 1989). Lifschitz & Hameiri (1991) investigated the asymptotic instability features, considering the initial value problem for the LEes and for the linearized equations of gas dynamics. Their more general approach was able to include both exponential and algebraic growth in time. Many efforts have since been made to quantitatively link the short-wave asymptotics and the normal-mode analysis: Sipp, Lauga & Jacquin (1999) showed agreement between the optimal streamline (i.e. the streamline where the inviscid growth rate is maximum) and the spatial distribution of the unstable eigenmodes, and between the inviscid and viscous amplification rate of an elliptic instability. Gallaire, Marquillie & Ehrenstein (2007) examined the centrifugal instability of the separated region behind a bump and were able to make a composite estimation of the growth rate taking into account the viscous effects (see also Landman & Saffman 1987) and the short-wave inviscid asymptotic limit. Recently, Giannetti (2015) applied a WKBJ approach to investigate the nature of the secondary instability arising in the periodic wake of a cylinder.

In this context, the main goal of the present work is to characterize the instabilities of the flow past an open cavity, develop an asymptotic approach to understand the instability mechanisms and finally relate the results of the global and local asymptotic analysis. The specific aims of the work, defining the outline of the article, are to:

(i) provide an accurate estimation of the critical Reynolds number and the spanwise wavenumber of the first three-dimensional bifurcation in incompressible open cavity flows;
(ii) determine the instability core by means of the adjoint-based structural sensitivity analysis;
(iii) investigate the sensitivity of the leading instability to base flow modifications induced by a perturbation of the inflow profile or wall blowing/suction;
(iv) provide a quantitative prediction of the onset of the instability by means of the short-wave asymptotic theory;
(v) show that the inviscid structural sensitivity (i.e. structural sensitivity based on direct and adjoint eigenmodes computed at a Reynolds number higher than that of the base flow) is able to accurately predict the particle orbit that provides the main contribution to the instability;
(vi) suggest a generalization of the expression used to calculate the instability growth rate from the Floquet exponent to predict the frequency of the time-dependent modes emerging at supercritical conditions.

2. Theoretical framework

2.1. *Geometrical configuration and base flow*

We investigate the stability and sensitivity of the flow over a spanwise-uniform square open cavity exposed to a uniform stream. The geometry, the frame of reference and the notation adopted in this work are all displayed in figure 1. The origin of the Cartesian reference system is located on the left edge of the cavity with x, y and z denoting the streamwise, wall-normal and spanwise directions. The fluid motion is described by the unsteady incompressible Navier–Stokes equations,

$$\boldsymbol{\nabla}\cdot\boldsymbol{u}=0, \tag{2.1a}$$

$$\frac{\partial \boldsymbol{u}}{\partial t}+(\boldsymbol{u}\cdot\boldsymbol{\nabla})\boldsymbol{u}=-\boldsymbol{\nabla}P+\frac{1}{Re_{BF}}\nabla^2\boldsymbol{u}, \tag{2.1b}$$

where $\boldsymbol{u}$ is the velocity vector with components $\boldsymbol{u}=(u, v, w)$ and P is the reduced pressure. Equations (2.1) are made dimensionless using the cavity depth D as the characteristic length scale and the velocity of the incoming uniform stream U_∞ as the reference velocity. The Reynolds number is thus defined as $Re_{BF}=U_\infty D/\nu$ (here the subscript BF means base flow Reynolds number) with ν the fluid kinematic viscosity. To ease comparisons, we have chosen the same boundary conditions as Sipp & Lebedev (2007) and Barbagallo, Sipp & Schmid (2009). The system of differential equations (2.1) is closed by the following Dirichlet boundary conditions at the inflow $\partial\mathscr{D}_{in}$ and stress-free conditions at the outflow $\partial\mathscr{D}_{out}$:

$$\boldsymbol{u}=1\cdot\boldsymbol{e}_x,\quad x\in\partial\mathscr{D}_{in};\qquad P\boldsymbol{n}-Re^{-1}(\boldsymbol{\nabla u})\cdot\boldsymbol{n}=\boldsymbol{0},\quad x\in\partial\mathscr{D}_{out}, \tag{2.2a,b}$$

where e_x is the unit vector in the direction of the x axis, n is the normal vector (in this case, it is the vector perpendicular to the outlet of the computational domain). Symmetric conditions (i.e. $\partial_y u=0$ and $v=0$) are imposed at the free-stream upper boundary of the computational domain $\partial\mathscr{D}_{ext}$ and no-slip conditions $\boldsymbol{u}=\boldsymbol{0}$ at the solid walls $\partial\mathscr{D}_w$. Note that a free-slip condition with zero tangential stress (i.e. $\partial_y u=0$ and $v=0$) is used on the walls close to the inflow and outflow $\partial\mathscr{D}_{fs}=\partial\mathscr{D}_{fs}^1\cup\partial\mathscr{D}_{fs}^2$.

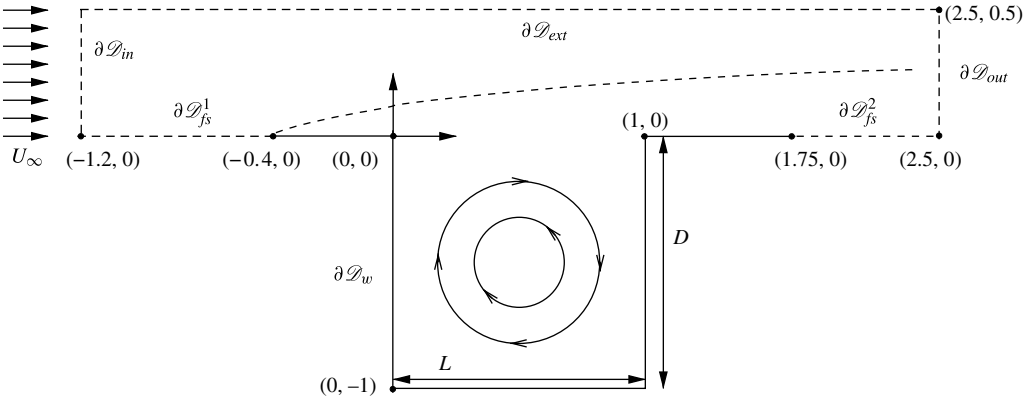

FIGURE 1. Flow configuration, frame of reference and computational domain $\mathscr{D}$. The main features of the flow are also sketched in the figure, i.e. the boundary layer developing over the walls, the shear layer above the cavity and the recirculation forming inside the cavity of length L and depth $D = L$.

2.2. *Global stability analysis*

The flow linear instability is studied with a classical normal-mode analysis. The analysis relies on the existence of a steady solution about which infinitesimal perturbations are superimposed. The velocity and pressure fields are decomposed into a two-dimensional base flow, $\boldsymbol{Q}_b(x, y) = (\boldsymbol{u}_b, P_b)^{\mathrm{T}} = (u_b, v_b, 0, P_b)^{\mathrm{T}}$, and a three-dimensional disturbance flow denoted by $\boldsymbol{q}'(x, y, z, t) = (\boldsymbol{u}', P')^{\mathrm{T}} = (u', v', w', P')^{\mathrm{T}}$ of small amplitude ϵ. Introducing this decomposition into (2.1) and linearizing the equations governing the disturbance evolution, we obtain the two systems describing the spatial structure of the base flow and the behaviour of generally unsteady perturbations. In particular, the base flow is governed by the steady version of (2.1), whereas the perturbation field is described by the linearized unsteady Navier–Stokes equations (LNSE)

$$\frac{\partial \boldsymbol{u}'}{\partial t} + \boldsymbol{L}\{\boldsymbol{u}_b(Re_{BF}), Re_{STB}\}\boldsymbol{u}' = -\boldsymbol{\nabla} P', \tag{2.3}$$

$$\boldsymbol{\nabla} \cdot \boldsymbol{u}' = 0, \tag{2.4}$$

with the linearized Navier–Stokes operator $\boldsymbol{L}$ (Re_{STB} indicates the Reynolds number used for stability computations)

$$\boldsymbol{L}\{\boldsymbol{u}_b, Re_{STB}\}\boldsymbol{u}' = \boldsymbol{u}_b \cdot \boldsymbol{\nabla}\boldsymbol{u}' + \boldsymbol{u}' \cdot \boldsymbol{\nabla}\boldsymbol{u}_b - \frac{1}{Re_{STB}}\nabla^2\boldsymbol{u}'. \tag{2.5}$$

As the base flow is homogeneous and stationary in the spanwise direction, a generic perturbation can be decomposed into Fourier modes of spanwise wavenumber k. The three-dimensional perturbations are expressed as

$$\boldsymbol{q}'(x, y, z, t) = \tfrac{1}{2}\{(\hat{u}, \hat{v}, \hat{w}, \hat{P})(x, y)\ \exp[\mathrm{i}kz + \gamma t] + \text{c.c.}\}, \tag{2.6}$$

where $\gamma = \eta + \mathrm{i}\omega$ is the complex growth rate and c.c. stands for complex conjugate. The real part η of γ represents the temporal growth rate of the perturbation and the

imaginary part ω its frequency. For $\eta > 0$, the flow is unstable whereas for $\eta < 0$ it is stable. Introducing the ansatz (2.6) in the LNSE (2.3)–(2.4), we obtain the generalized eigenvalue problem

$$\boldsymbol{A}\hat{\boldsymbol{q}} + \gamma \boldsymbol{B}\hat{\boldsymbol{q}} = 0, \tag{2.7}$$

in which $\hat{\boldsymbol{q}} = (\hat{u}, \hat{v}, \hat{w}, \hat{P})^{\mathrm{T}}$ and $\mathscr{A}$ is the complex linearized evolution operator. The operators $\mathscr{A}$ and $\mathscr{B}$, have the following expressions:

$$\boldsymbol{A} = \begin{pmatrix} \mathscr{C} - \mathscr{M} + \partial_x u_b & \partial_y u_b & 0 & \partial_x \\ \partial_x v_b & \mathscr{C} - \mathscr{M} + \partial_y v_b & 0 & \partial_y \\ 0 & 0 & \mathscr{C} - \mathscr{M} & \mathrm{i}k \\ \partial_x & \partial_y & \mathrm{i}k & 0 \end{pmatrix}, \quad \boldsymbol{B} = \begin{pmatrix} 1 & 0 & 0 & 0 \\ 0 & 1 & 0 & 0 \\ 0 & 0 & 1 & 0 \\ 0 & 0 & 0 & 0 \end{pmatrix}, \tag{2.8a,b}$$

where $\mathscr{M} = {Re_{STB}}^{-1}(\partial_{x^2} + \partial_{y^2} - k^2)$ and $\mathscr{C} = u_b\partial_x + v_b\partial_y$ describe the viscous diffusion of the perturbation and its advection by the mean flow. The boundary conditions associated with the eigenproblem (2.7) are derived from those used for the base flow, i.e.

$$\hat{\boldsymbol{u}} = \boldsymbol{0}, \quad \text{on } \partial\mathscr{D}_{in} \cup \partial\mathscr{D}_{w} \text{ (inlet and wall)}, \tag{2.9a}$$

$$\hat{P}\boldsymbol{n} - {Re_{STB}}^{-1}(\boldsymbol{\nabla}\hat{\boldsymbol{u}}) \cdot \boldsymbol{n} = \boldsymbol{0}, \quad \text{on } \partial\mathscr{D}_{out} \text{ (outlet)}, \tag{2.9b}$$

$$\partial_y\hat{u} = \hat{v} = \hat{w} = 0, \quad \text{on } \partial\mathscr{D}_{ext} \cup \partial\mathscr{D}_{fs} \text{ (free stream and free-slip boundary)}. \tag{2.9c}$$

Finally, we note that the complex-conjugate pairs $(\eta + \mathrm{i}\omega; \hat{\boldsymbol{q}})$ and $(\eta - \mathrm{i}\omega; \hat{\boldsymbol{q}}^*)$ are both solutions of the eigenproblem (2.7) with the boundary conditions (2.9) for a real base flow $\boldsymbol{Q}_b$. Thus, the eigenvalues are complex conjugates and the spectra are in a symmetric plane with respect to the real axis in the (η, ω).

2.3. *Determination of the instability core: structural sensitivity*

In this section we present the structural sensitivity analysis following the framework in Pralits, Brandt & Giannetti (2010). The underlying idea is the concept of 'wavemaker', introduced by Giannetti & Luchini (2007) to identify the location of the core of a global instability. The wavemaker is the region in the flow where variations in the structure of the problem provide the largest drift of a specific eigenvalue. We first consider the perturbed eigenvalue problem

$$\gamma'\hat{\boldsymbol{u}}' + \boldsymbol{L}\{\boldsymbol{u}_b, Re_{STB}\}\hat{\boldsymbol{u}}' = -\boldsymbol{\nabla}\hat{P}' + \delta\boldsymbol{H}(\hat{\boldsymbol{u}}', \hat{P}'), \tag{2.10}$$

$$\boldsymbol{\nabla} \cdot \hat{\boldsymbol{u}}' = 0, \tag{2.11}$$

where $\delta\boldsymbol{H}$ is the generalized structural perturbation. It is assumed to be a momentum force localized in space and proportional to the local velocity perturbation through a (3×3) coupling matrix $\delta\boldsymbol{M}_0$ and a Dirac delta function:

$$\delta\boldsymbol{H}(\hat{\boldsymbol{u}}', \hat{P}') = \delta\boldsymbol{M}(x, y) \cdot \hat{\boldsymbol{u}}' = \delta(x - x_0, y - y_0)\delta\boldsymbol{M}_0 \cdot \hat{\boldsymbol{u}}'. \tag{2.12}$$

Neglecting higher-order terms, variations of the eigenvalue $\delta\gamma$ and of the corresponding eigenfunction $(\delta\hat{\boldsymbol{u}}, \delta\hat{P})$ satisfy the following expressions:

$$\gamma\delta\hat{\boldsymbol{u}} + \boldsymbol{L}\{\boldsymbol{u}_b, Re_{STB}\}\delta\hat{\boldsymbol{u}} = -\boldsymbol{\nabla}\delta\hat{P} + \delta\boldsymbol{M} \cdot \hat{\boldsymbol{u}} - \delta\gamma\hat{\boldsymbol{u}}, \tag{2.13}$$

$$\boldsymbol{\nabla} \cdot \delta\hat{\boldsymbol{u}} = 0. \tag{2.14}$$

Using then the Lagrange identity (see Luchini & Bottaro 2014), we can determine the equations governing the structure of the adjoint field: $\hat{\boldsymbol{g}}^+(x, y) = (\hat{\boldsymbol{f}}^+, \hat{m}^+)$

$$-\gamma\hat{\boldsymbol{f}}^+ + \boldsymbol{u}_b \cdot \nabla\hat{\boldsymbol{f}}^+ - \nabla\boldsymbol{u}_b \cdot \hat{\boldsymbol{f}}^+ + \frac{1}{Re_{STB}}\nabla^2\hat{\boldsymbol{f}}^+ + \nabla\hat{m}^+ = 0, \tag{2.15}$$

$$\nabla \cdot \hat{\boldsymbol{f}}^+ = 0. \tag{2.16}$$

After integration over the domain $\mathscr{D}$, accounting for the boundary conditions and introducing the sensitivity tensor

$$\boldsymbol{S}(x_0, y_0; Re_{BF}, Re_{STB}) = \frac{\hat{\boldsymbol{f}}^+(x_0, y_0)\hat{\boldsymbol{u}}(x_0, y_0)}{\displaystyle\int_{\mathscr{D}} \hat{\boldsymbol{f}}^+ \cdot \hat{\boldsymbol{u}}\,\mathrm{d}S}, \tag{2.17}$$

we can express the eigenvalue drift due to the local feedback as

$$\delta\gamma(x_0, y_0) = \frac{\displaystyle\int_{\mathscr{D}} \hat{\boldsymbol{f}}^+ \cdot \delta\boldsymbol{M} \cdot \hat{\boldsymbol{u}}\,\mathrm{d}S}{\displaystyle\int_{\mathscr{D}} \hat{\boldsymbol{f}}^+ \cdot \hat{\boldsymbol{u}}\,\mathrm{d}S} = \frac{\hat{\boldsymbol{f}}^+ \cdot \delta\boldsymbol{M}_0 \cdot \hat{\boldsymbol{u}}}{\displaystyle\int_{\mathscr{D}} \hat{\boldsymbol{f}}^+ \cdot \hat{\boldsymbol{u}}\,\mathrm{d}S} = \boldsymbol{S} : \delta\boldsymbol{M}_0 = \sum_{ij} S_{ij}\delta M_{0ij}. \tag{2.18}$$

Different norms of the tensor $\boldsymbol{S}$ can be used to build a spatial map of the sensitivity. The spectral norm is chosen here to study the worst possible case.

3. Numerical approach

3.1. *Base flow calculation*

The numerical computation of the base flow has been performed using a finite element method. The variational formulation of the Navier–Stokes equations (2.1) is implemented in the software package FreeFem++ (Hecht (2012); http://www.freefem.org) using classical $P2$–$P1$ Taylor–Hood elements for the spatial discretization. The resultant nonlinear system of algebraic equations, along with the boundary conditions, is solved by a Newton–Raphson procedure: given an initial guess $\boldsymbol{w}_b{}^{(0)}$, the linear system

$$NS(Re_{BF}, \boldsymbol{W}_b{}^{(n)}) \cdot \boldsymbol{w}_b{}^{(n)} = -rhs^{(n)} \tag{3.1}$$

is solved at each iteration step using the MUMPS (multifrontal massively parallel sparse direct solver) (Amestoy *et al.* 2001, 2006) for the matrix inversion. The base flow is then updated as

$$\boldsymbol{W}_b^{(n+1)} = \boldsymbol{W}_b{}^{(n)} + \boldsymbol{w}_b{}^{(n)}. \tag{3.2}$$

The initial guess is chosen to be the solution of the Stokes equations and the process is continued until the L^2-norm of the residual of the governing equations becomes smaller than 10^{-12}. To test the implementation and convergence, we used three different meshes M1, M2 and M3 (see table 1). These are generated by the bidimensional anisotropic mesh generator (Bamg) that is part of the Freefem++ package. The base flow computations are also validated using a variant of the second-order finite-difference code described in Giannetti & Luchini (2007). A typical steady flow over the open cavity is depicted in figure 2.

Mesh	η	ω	$n_{d.o.f.}$	n_t	Source
M1	0.0007590	7.4931	998 668	221 045	Present
M2	0.0008344	7.4937	1416 630	313 791	Present
M3	0.0009122	7.4943	2601 757	576 887	Present
D1	0.0007401	7.4930	880 495	194 771	Sipp & Lebedev (2007)
D2	0.0008961	7.4942	1888 003	418 330	Sipp & Lebedev (2007)

TABLE 1. Comparison of the results obtained with the present implementation and those reported by Sipp & Lebedev (2007) for the same configuration. The eigenfrequency ω and the growth rate η have been calculated for the first two-dimensional unstable eigenmode at $Re_{BF} = Re_{STB} = 4140$; $n_{d.o.f.}$ and n_t indicate the total number of degrees of freedom of the linearized problem and the number of triangles for each of the unstructured meshes used.

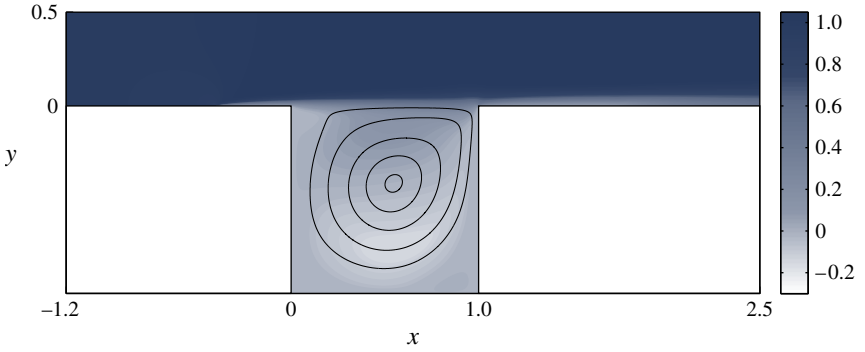

FIGURE 2. (Colour online) Visualization of the steady two-dimensional base flow for the Reynolds number $Re_{BF} = 1370$ at which a three-dimensional instability is first observed. The background shading displays the streamwise velocity whereas solid lines indicate the streamlines inside the cavity.

3.2. *Eigenvalue solver and adjoint field*

Once the base flow is determined, the system (2.7) is used to perform the stability analysis. After spatial discretization, the governing equations and their boundary conditions (2.9) are recast in the following standard form:

$$[\boldsymbol{A}(Re_{STB}, \boldsymbol{W}_b(Re_{BF})) + \gamma \boldsymbol{B}] \cdot \boldsymbol{w} = \boldsymbol{0}, \tag{3.3}$$

where $\boldsymbol{w}$ is the right (or direct) eigenvector. As methods based on the QR decomposition are not feasible for solving large-scale problems like those associated with the matrix $\boldsymbol{A}$ obtained for our problem, we adopt an efficient matrix-free iterative method based on the Arnoldi algorithm (Arnoldi 1951). We use the state-of-the-art ARPACK package (Lehoucq *et al.* 2007), with implicit restarts to limit memory requirements. The solution of the linear system built by the Arnoldi iterations on the Krylov subspace is obtained with the same sparse solver (Amestoy *et al.* 2001, 2006) as used for the base flow calculations. The adjoint modes are computed as left eigenvectors of the discrete system derived from the discretization of the linearized equations and the sensitivity function is then computed by the product of the direct

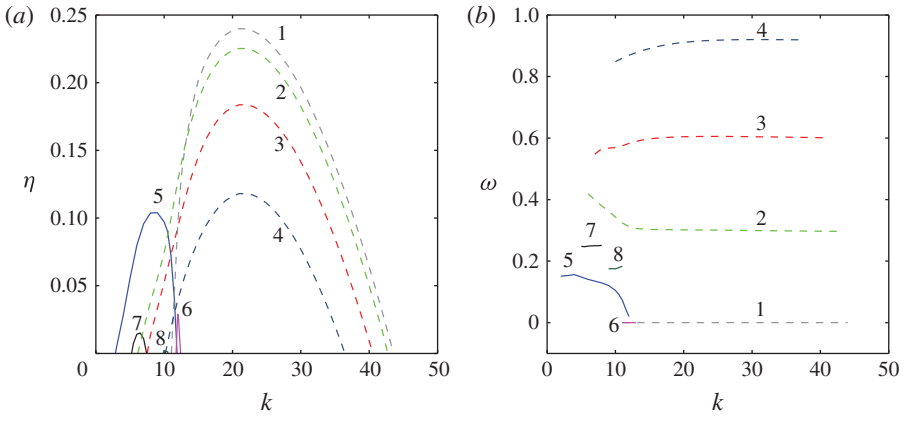

FIGURE 3. (Colour online) Stability analysis of the open cavity flow at $Re = 4140$, where an unstable two-dimensional mode first emerges. (*a*) Real and (*b*) imaginary part of the eigenvalue γ versus the spanwise wavenumber k. The different branches are numbered for future reference.

and the adjoint fields. The right (direct) and left (adjoint) eigenvectors are normalized by requiring

$$\max_{x,y\in\mathscr{D}}\{|\hat{u}(x,y)|\} = 1, \qquad \int_{\mathscr{D}} \hat{\boldsymbol{f}}^{+} \cdot \hat{\boldsymbol{u}} \mathrm{d}S = 1. \tag{3.4a,b}$$

The code is validated against the results reported by Sipp & Lebedev (2007). These authors investigate the stability of a Newtonian fluid in the same geometrical configuration and report the first instability of a two-dimensional eigenmode to occur at $Re = 4140$. In table 1 we present the comparison between our results and the results in Sipp & Lebedev (2007) for different meshes. In these tests, 50 eigenvalues were obtained, with an initial Krylov basis of dimension 150; the convergence criterion for the Arnoldi iterations is based on a tolerance of 10^{-9}. To independently check the accuracy of the results we *a posteriori* computed the residual $\max_i |(A_{ij} + \gamma B_{ij})w_j|$: this turns out to be always below 10^{-9} for the results reported in this paper, typically less than 10^{-12} for the least stable modes. The majority of the computations presented in the following are obtained using mesh M2. Henceforth whenever $Re_{BF} = Re_{STB}$ we will simply use Re.

4. Linear stability results

4.1. *Three-dimensional versus two-dimensional instability*

As the cavity is typically considered an example of centrifugal instability, we expect the first bifurcation to be characterized by the appearance of steady three-dimensional modes of relatively short wavelength in the spanwise direction (Albensoeder, Kuhlmann & Rath 2001). To verify this, we scan the k-axis seeking for unstable modes at the Reynolds number $Re = 4140$ where a two-dimensional mode first becomes unstable (Sipp & Lebedev 2007). The results in figure 3 clearly show that eight unstable branches can be found for this value of Re where the most unstable mode has wavenumber $k = 22$ and represents a steady disturbance ($\omega = 0$ in figure 3*b*). The flow over an open cavity is therefore characterized by a first bifurcation to a steady three-dimensional configuration.

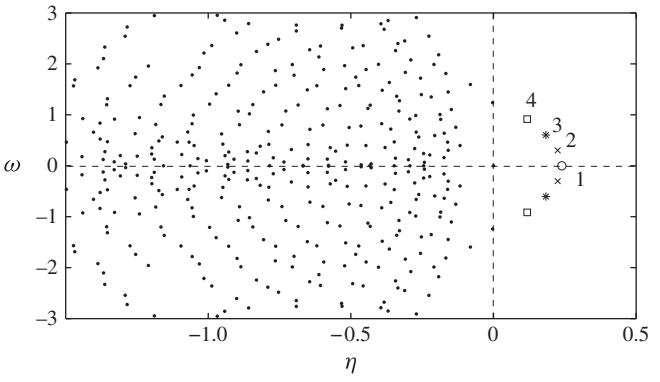

FIGURE 4. Eigenvalue spectrum for $Re = 4140$ and $k = 22$. The numbers in the figure relates to the branches identified in figure 3.

The full eigenvalue spectrum at $k = 22$ is shown in figure 4 where seven unstable modes appear (four branches with respect to k), placed symmetrically with respect to the real axis. It is interesting to highlight that the steady mode is the most unstable one, while the others are characterized by frequencies which are integer multiples of a fundamental one and arise (as explained in § 7) as results of resonances on a particular streamline.

In figure 5 we display the modulus of both the direct and adjoint eigenfunctions corresponding to the eigenvalues denoted by 1, 2, 3, and 4 in figure 4. The velocity perturbations are most evident in the circular region inside the cavity, with a tail in the shear region just above the downstream wall. The adjoint modes, indicating the region in the flow most receptive to forcing in the momentum equations, have a similar structure, except for the thin region close to the upstream tip of the cavity, where instability is most efficiently triggered. The unstable modes are spatially localized in the same region. The secondary flow generated by the leading instability can be described as a flat roll lying within the square cavity. The different resonances are associated with periodic oscillations again concentrated in the region inside the cavity.

To document the appearance of this two-to-three-dimensional bifurcation, we determine the critical Reynolds number at which the instability first occurs: as shown in figure 6 the critical value is about $Re_{cr} \approx 1370$ and the first mode to become unstable is associated with a wavenumber $k \approx 13.4$. All modes whose growth rate is reported in figure 6 have zero frequency; this stationary instability will be analysed in detail in the rest of the paper.

4.2. *Structural sensitivity of the first bifurcation*

We study the characteristics of the bifurcation by first showing the spatial structure of the fluctuation of the least stable mode at $Re = 1370$, $k = 13.4$. Like the modes at higher Reynolds number, the mode is localized along the external streamlines of the recirculation region inside the cavity (see figure 7). The level of fluctuations is largest in the streamwise component, the cross-stream and spanwise ones being respectively about 61 % and 88 % of the streamwise fluctuations. The adjoint of the critical mode is displayed in figure 7(*d–f*): its spatial structure closely resembles that of the direct mode, with a strong localization along the circular streamlines inside the cavity. As noted above, the direct mode presents a second region of noticeable amplitude near the

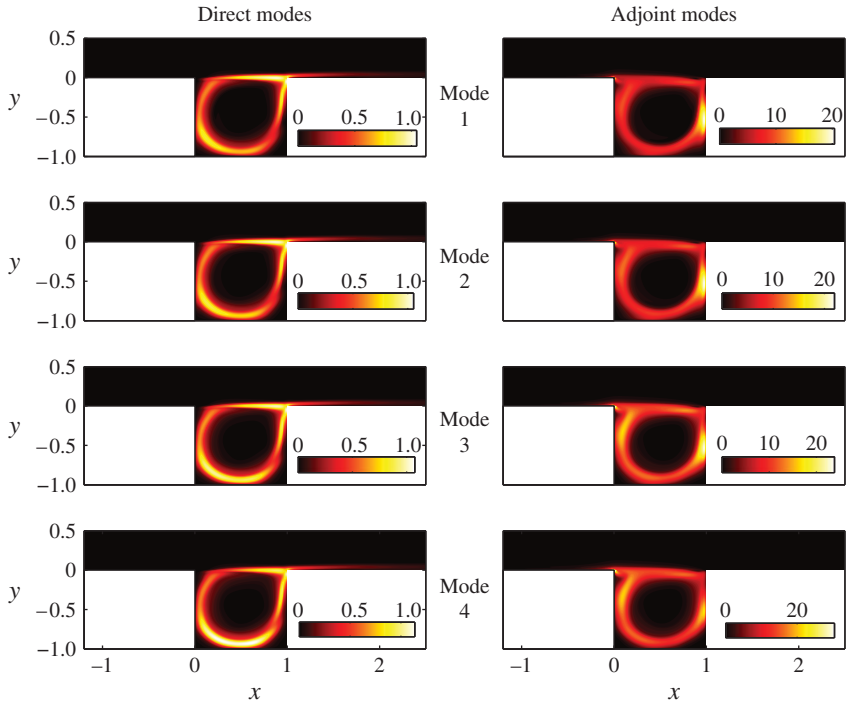

FIGURE 5. (Colour online) Contour plots of the absolute value of the direct and adjoint eigenfunctions of modes 1, 2, 3 and 4 as denoted in figure 4 for $Re = 4140$ and $k = 22$. Global mode 1 is stationary ($\omega = 0$), mode 2 has $\omega \approx 0.3$, mode 3 has $\omega \approx 0.6$ and mode 4 has $\omega \approx 0.9$.

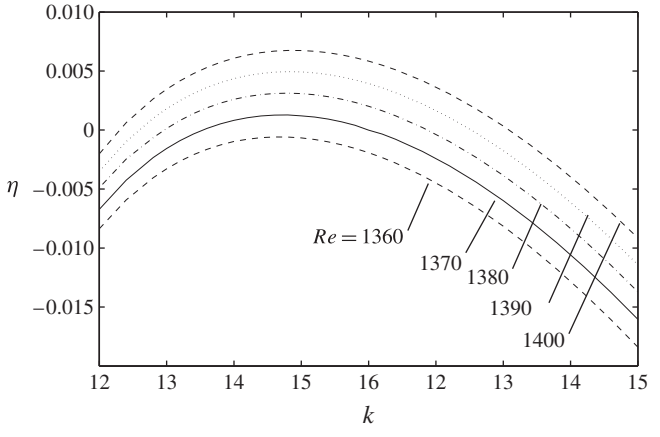

FIGURE 6. Leading eigenmode for cavity flow with $L/D = 1$. Growth rate of the most unstable mode versus the spanwise wavenumber k for the Reynolds numbers indicated. The circular frequency is zero for all modes displayed. Thus, the first instability of the flow over an open cavity is a three-dimensional steady mode.

downstream tip of the cavity and in the shear region just downstream of it, whereas the amplitude of the adjoint mode is not negligible near the upstream tip.

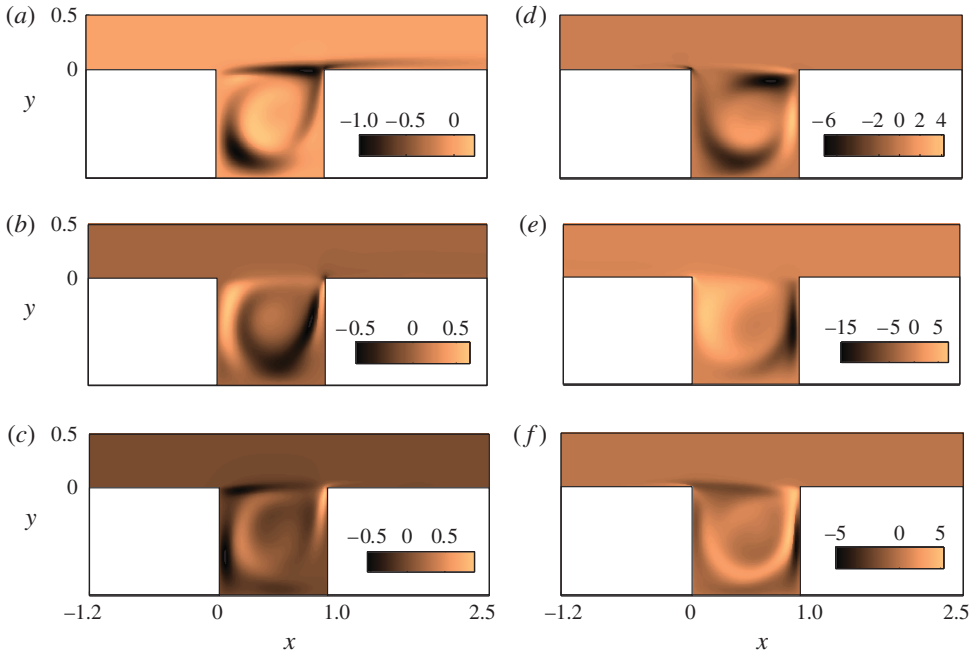

FIGURE 7. (Colour online) Contour plots of the streamwise (*a* direct; *d* adjoint), wall-normal (*b* direct; *e* adjoint) and spanwise (*c* direct; *f* adjoint) component of the direct and adjoint mode close to the critical Reynolds number $Re = 1370$, $k = 13.4$.

The structural sensitivity of this mode is displayed in figure 8. This quantity indicates the regions in the flow where a feedback forcing proportional to the local perturbation velocity most alters the eigenvalue, in other words the wavemaker of the instability. The sensitivity, product of the direct and adjoint mode, is largest inside the cavity, with no significant contributions from the regions of strong shear above it. It is interesting to note that the wavemaker is similar to that computed for a lid-driven square cavity (Giannetti, Luchini & Marino 2010; Haque *et al.* 2012).

5. Instabilities in cavity flows

5.1. *Open cavity and lid-driven cavity*

The sensitivity analysis performed in the previous section clearly shows that the core of the three-dimensional instability leading to the first bifurcation in a square open cavity is highly localized in space and completely contained inside the cavity. This is in contrast with the first 2D instability (Sipp & Lebedev 2007), arising at $Re = 4140$, which is more similar to a wake-type instability (Sipp 2012; Yamouni *et al.* 2013) and localized downstream near the second tip of the cavity.

Examining the results obtained from the stability analysis, it is clear that the external flow plays little role in the generation mechanism of the three-dimensional instability. It is thus reasonable to assume that the configuration studied here is subject to the same type of instabilities as those appearing in a LDC and discussed by Albensoeder *et al.* (2001) and Albensoeder & Kuhlmann (2006) among others. In the open cavity the shear layer detaching from the upstream corner has the same role as that of the lid in the formation of the vortical motion inside the LDC configuration.

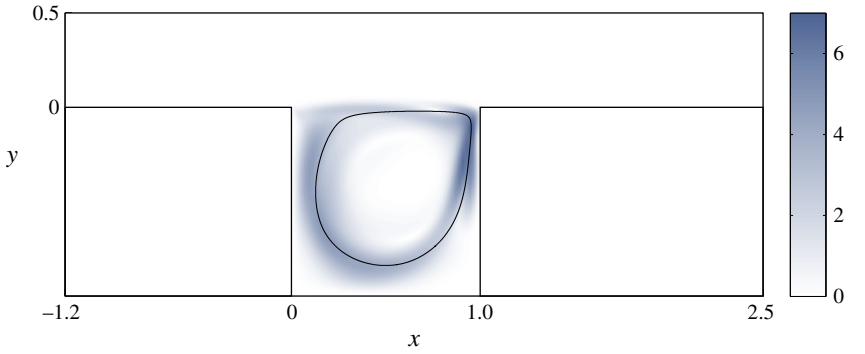

FIGURE 8. (Colour online) Structural sensitivity, the core of the instability, at the neutral conditions, $Re = 1370$, $k = 13.4$, for the flow over an open square cavity. The streamline where the asymptotic analysis predicts the maximum inviscid growth rate is also depicted (see § 7).

The velocity of the lid is uniform while in the present study the fluid velocity along the line connecting the two upper corners is not constant: the velocity starts from zero at the left corner, increases, reaches a maximum and then decreases again, vanishing at the downstream corner. In addition, the vertical velocity is different from zero, its magnitude being smaller than that of the horizontal component, however. As a result the flow field, although qualitatively similar, also has important differences with respect to that occurring in the lid-driven problem.

For the LDC the critical Reynolds number for the first bifurcation has been calculated independently by Theofilis (2000) and Albensoeder *et al.* (2001) (see also Ding & Kawahara 1998; Shatrov, Mutschke & Gerbeth 2003). The numerical three-dimensional linear stability analysis of Albensoeder *et al.* (2001) covers a wide range of cavity aspect ratios and presents the corresponding unstable modes, which appear to be qualitatively different when varying the cavity aspect ratio. These authors explain the centrifugal instability mechanism in terms of the perturbation energy budget and the criterion proposed by Sipp & Jacquin (2000).

As suggested by Brés & Colonius (2008) (see § 4.2 of their paper), if we introduce a (base flow) Reynolds number Re_{av} based on the cavity depth D and on the average velocity $\tilde{U}$ along the line connecting the two opposite corners, the critical Reynolds number for the first instability of the open cavity flow becomes

$$Re_{av} = \frac{\tilde{U}D}{\nu} \approx 490, \tag{5.1}$$

which is around 38 % lower than the value found by Albensoeder *et al.* (2001). Despite this difference in the value of the critical Reynolds number, the spanwise wavenumbers at which the instability first occurs are comparable, being $k_{lid} \approx 15.4$ in the LDC case and $k \approx 13.4$ in the present configuration. These qualitative similarities, both in terms of base flows and modes, suggest that the same kind of instability is acting in the two configurations.

5.2. *Link between open cavity flows*

Brés & Colonius (2008) performed DNS of open cavity flows for several Re_{δ^*}, where δ^* is displacement thickness, to investigate the effect of this parameter on the

instability properties. In the present configuration the shear layer starts developing at $x^{bl} = -0.4$ (we recall that the origin of our frame of reference is located on the left edge of the cavity) leading to a displacement thickness at the upstream edge of ($Re = 1370$)

$$\delta^*(x^{bl}) = \int_0^{0.5} \frac{u_b(x^{bl}, 0.5) - u_b(x^{bl}, y)}{u_b(x^{bl}, 0.5)} \mathrm{d}y \approx 0.029. \tag{5.2}$$

Thus, the critical Reynolds number based on this boundary-layer thickness is equal to $Re_{\delta^*} = U_\infty \delta^*(x^{bl})/\nu \approx 39.7$.

As discussed in Brés & Colonius (2008), the critical conditions for the instability are only weakly affected by the starting position of the upstream laminar boundary layer when the critical Reynolds number is appropriately defined. The main idea is that the dynamics inside the cavity is approximately driven by the average velocity between the two edges rather than by the shear-layer thickness, thus strengthening the connection to the LDC flow. Analysing the limiting case arising when the incoming free-stream velocity U_∞ is simply linear, i.e. when a Couette profile of velocity $U_\infty(y) = \boldsymbol{y} \cdot \boldsymbol{e_y}$ is imposed at the inlet, we found that the first bifurcation occurs at $Re^{Couette} \approx 20\,200$ for modes of spanwise wavenumber $k \approx 13.0$. Interestingly, the critical Reynolds number scaled with the cavity depth and average velocity, $Re_{av} \approx 470$, is in a very good agreement with the value obtained previously, (5.1), although the boundary-layer thickness of Couette flow is infinity. In the light of this result we confirm that the averaged Reynolds number Re_{av} is a relevant parameter to predict the onset of instability for open cavity flows.

6. Structural sensitivity to a velocity-based linear feedback

The so-called sensitivity to base flow variations is a concept introduced by Bottaro, Corbett & Luchini (2003) and Marquet, Sipp & Jacquin (2008) within the global framework. In this analysis a small structural velocity-based perturbation acts at the base flow level: the effect of the base flow modifications on the leading eigenvalue of the stability problem allows us to study the different mechanisms that can suppress or enhance the instability. The spatial structure of the so-called adjoint base flow can be used to identify the features of the base flow that provide the main contribution to the instability dynamics and the regions where to locate effective passive control devices. In other words, this modification of the structure of the Navier–Stokes operator causes a variation of the base flow which in turn produces a drift of the leading eigenvalue $\gamma = \eta + \mathrm{i}\omega$.

For the sake of brevity, only the main ingredients are outlined here; an extensive and detailed derivation can be found in Marquet *et al.* (2008) and Pralits *et al.* (2010). Using a formalism based on control theory, the eigenproblem (2.7) represents the state equation, the state vector is composed of the global mode $\hat{\boldsymbol{q}}$ and the complex eigenvalue γ, and the base flow $\boldsymbol{Q}_b$ is the control variable. As in Pralits *et al.* (2010) we express the eigenvalue drift $\delta\gamma$ as

$$\delta\gamma = \delta\eta + \mathrm{i}\delta\omega = \frac{\displaystyle\int_{\mathscr{D}} (\hat{\boldsymbol{u}} \cdot \nabla \hat{\boldsymbol{f}}^+ - \nabla \hat{\boldsymbol{u}} \cdot \hat{\boldsymbol{f}}^+) \cdot \delta \boldsymbol{u}_b \mathrm{d}S}{\displaystyle\int_{\mathscr{D}} \hat{\boldsymbol{f}}^+ \cdot \hat{\boldsymbol{u}} \mathrm{d}S}, \tag{6.1}$$

where $\delta\boldsymbol{u}_b$ is a generic modification of the base flow. The relation (6.1) provides the effect of a specified velocity distribution implying a dedicated computation for

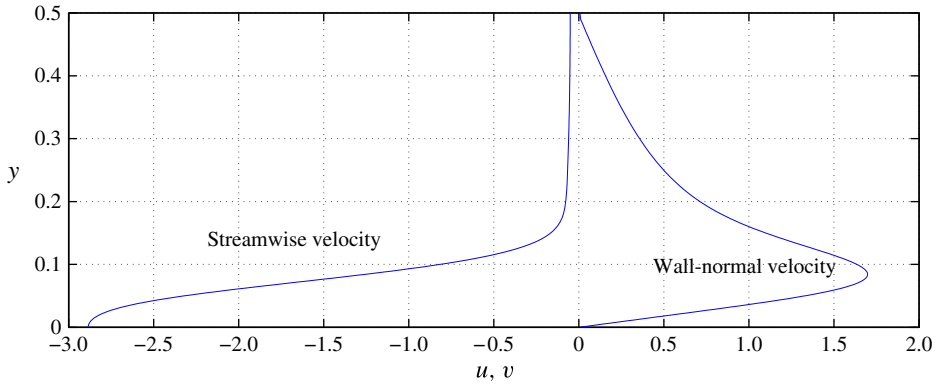

FIGURE 9. (Colour online) Sensitivity of the first bifurcation to streamwise and wall-normal mean velocity modifications at the inflow. The profile shown would provide the largest possible stabilization of the first bifurcation.

each specific actuation, e.g. wall blowing/suction. The optimal boundary velocity distribution, instead, can be directly found as follows (see Meliga & Chomaz 2011):

$$\delta\gamma = \frac{\displaystyle\int_{\partial\mathscr{D}_{w,i,fs}} \left[\left(m_b^+\boldsymbol{n} + \frac{1}{Re}\boldsymbol{n}^{\mathrm{T}}\cdot\boldsymbol{\nabla}\boldsymbol{f}_b^+\right)\cdot\delta\,\boldsymbol{U}_{w,i,fs}\right]\mathrm{d}l}{\displaystyle\int_{\mathscr{D}} \hat{\boldsymbol{f}}^+\cdot\hat{\boldsymbol{u}}\,\mathrm{d}S} \tag{6.2}$$

where m_b^+ and $\hat{\boldsymbol{f}}_b^+$ are the adjoint base flow pressure and the three-dimensional adjoint base flow velocity field and the subscripts w, i, fs indicate the boundaries (inlet, wall or free-slip) on which we calculate the integral $\mathrm{d}l$ is the length element along $\partial D_{w,i,fs}$. The adjoint base flow field $\boldsymbol{Q}_b^+$ must satisfy the following set of linear equations (Pralits *et al.* 2010):

$$\boldsymbol{u}_b\cdot\boldsymbol{\nabla}\boldsymbol{f}_b^+ - \boldsymbol{\nabla}\boldsymbol{u}_b\cdot\boldsymbol{f}_b^+ + \frac{1}{Re}\nabla^2\boldsymbol{f}_b^+ + \boldsymbol{\nabla}m_b^+ = \hat{\boldsymbol{u}}\cdot\boldsymbol{\nabla}\hat{\boldsymbol{f}}^+ - \boldsymbol{\nabla}\hat{\boldsymbol{u}}\cdot\hat{\boldsymbol{f}}^+, \tag{6.3}$$

$$\boldsymbol{\nabla}\cdot\boldsymbol{f}_b^+ = 0, \tag{6.4}$$

along with the adjoint base flow outlet condition $m_b^+\boldsymbol{n} - Re^{-1}\boldsymbol{n}\cdot\boldsymbol{\nabla}\boldsymbol{f}_b^+ = -(\boldsymbol{u_b}\cdot\boldsymbol{n})\boldsymbol{f}_b^+ + (\hat{\boldsymbol{u}}\cdot\boldsymbol{n})\hat{\boldsymbol{u}}^+$ at $\partial\mathscr{D}_{out}$ and zero-velocity conditions at the solid walls and at the inlet.

The sensitivity of the instability with respect to the incoming flow is examined first. Figure 9 shows the sensitivity to both the streamwise and the wall-normal components of the inflow velocity profile, where the profiles shown would provide the optimal decrease of the instability growth rate. The x-component is found to be always negative and attains significant values only near the wall. This fact is not surprising because the base flow modifications have effect only if related to the shear layer that drives the core vortex inside the cavity. Perturbations in the free stream do not affect the flow at the edge and inside the cavity, the regions where the instability is triggered. Negative modifications of the inlet velocity profile cause stabilization due to decrease of the momentum inside the shear layer. The effect of the wall-normal component is related to the same mechanism, decreasing of the total streamwise momentum at the cavity tip by normal advection.

In view of an active control of the first bifurcation, we depict the wall-normal component of the sensitivity along the cavity walls in figure 10; this corresponds to

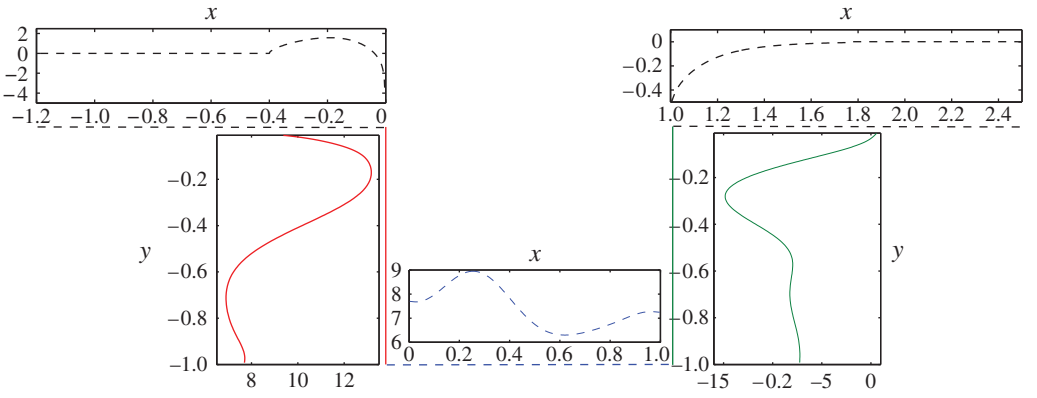

FIGURE 10. (Colour online) Sensitivity to wall-normal blowing and suction of the leading-mode growth rate at $Re = 1370$ and $k = 13.4$. Positive (negative) values indicate blowing (suction) and lead to stabilization (destabilization). The profiles shown on each wall provide the optimal decrease of the instability growth rate.

the optimal blowing/suction profiles giving the largest stabilization. We see that the sensitivity is vanishing along the first free-slip boundary just downstream of the inflow ($y = 0$; $-1.2 < x < -0.4$), while a combination of blowing and suction is found to be optimal on the wall upstream of the cavity ($y = 0$; $-0.4 < x < 0$). Inside the cavity, on both lateral walls, a stabilizing normal component is directed in the streamwise direction. The optimal blowing and suction on the lower wall would create a flow opposite to the vortex inside the cavity, thus trying to quench it. The analysis, finally, shows that it is not possible to significantly modify the instability by applying control on the downstream wall (lowest sensitivity magnitude).

7. Asymptotic inviscid stability theory

The spatial distribution of the structural sensitivity (that is spatially concentrated around a streamline inside the cavity) suggests the possibility of using the local theory to describe the evolution of the instability and provide more quantitative evidence for the mechanism from which it arises. An appealing approach in this context is offered by the short-wavelength approximation (WKBJ) developed by Bayly (1988).

This approach is briefly outlined here; for a more detailed presentation the reader is referred to Lifschitz & Hameiri (1991), Lifschitz (1994) and references therein. The solution of the linearized Navier–Stokes equations is sought in the form of a rapidly oscillating and localized wave-packet evolving along the Lagrangian trajectory $\boldsymbol{X}(t)$ and characterized by a wave-vector $\boldsymbol{k}(t) = \nabla\phi(\boldsymbol{X}, t)$ and an envelope $\boldsymbol{a}(\boldsymbol{X}, t)$ such that

$$\boldsymbol{u}(\boldsymbol{X}, t) = \mathrm{e}^{\mathrm{i}\phi(\boldsymbol{X},t)/\epsilon}\boldsymbol{a}(\boldsymbol{X}, t, \epsilon) = \mathrm{e}^{\mathrm{i}\phi(\boldsymbol{X},t)/\epsilon}\sum_n \boldsymbol{a}_n(\boldsymbol{X}, t)\epsilon^n, \tag{7.1}$$

$$p(\boldsymbol{X}, t) = \mathrm{e}^{\mathrm{i}\phi(\boldsymbol{X},t)/\epsilon}b(\boldsymbol{X}, t, \epsilon) = \mathrm{e}^{\mathrm{i}\phi(\boldsymbol{X},t)/\epsilon}\sum_n b_n(\boldsymbol{X}, t)\epsilon^{n+1}, \tag{7.2}$$

where $\epsilon \ll 1$ and $\boldsymbol{X} = \epsilon\boldsymbol{x}$ is a slowly varying variable. In the limit of vanishing viscosity ($Re \to \infty$) and large wavenumbers ($\|\boldsymbol{k}\| \to \infty$), the theory provides the leading-order term for the growth rate associated with a localized perturbation. This

is obtained by integrating the following set of ordinary differential equations (ODEs):

$$\frac{\mathrm{D}\boldsymbol{k}}{\mathrm{D}t} = -\boldsymbol{L}^t(\boldsymbol{X})\boldsymbol{k}, \tag{7.3}$$

$$\frac{\mathrm{D}\boldsymbol{a}}{\mathrm{D}t} = \left(\frac{2\boldsymbol{k}\boldsymbol{k}^{\mathrm{T}}}{|\boldsymbol{k}|^2} - \boldsymbol{I}\right)\boldsymbol{L}(\boldsymbol{X})\boldsymbol{a}, \tag{7.4}$$

along the Lagrangian trajectories defined by the ODE

$$\frac{\mathrm{D}\boldsymbol{X}(t)}{\mathrm{D}t} = \boldsymbol{u}_b(X(t), t). \tag{7.5}$$

In the equations above $\boldsymbol{L} = \nabla\boldsymbol{u}_b$ is the base flow velocity gradient tensor and $\boldsymbol{I}$ the identity matrix. Since the flow under investigation is steady, the Lagrangian trajectory corresponds to the streamlines of the base flow. Three initial conditions have to be assigned to solve the problem above: $\boldsymbol{k}(t=0) = \boldsymbol{k}_0$, $\boldsymbol{a}(t=0) = \boldsymbol{a}_0$ and $\boldsymbol{x}(t=0) = \boldsymbol{x}_0$. The last condition imposes the Lagrangian origin of the streamline and thereby entirely identifies it.

Lifschitz & Hameiri (1991) proved that a sufficient condition for inviscid instability is that the system (7.3)–(7.5) has at least one solution for which $\|\boldsymbol{a}(t)\| \to \infty$ as $t \to \infty$. This theory has been successfully applied in the past to study elliptic, hyperbolic and centrifugal instabilities of two-dimensional stationary base flows (Sipp *et al.* 1999; Godeferd, Cambon & Leblanc 2001). In order to characterize the instability mechanism arising inside the cavity with this local theory, the self-excited nature of the instability must be properly accounted for. In this context, a central role is played by closed Lagrangian trajectories (closed streamlines in our case), i.e. orbits described by material points which return to their initial positions after a given time T (the period of revolution of a material particle). These closed trajectories play a special role in the dynamics of the instability: on the closed orbits, local instability waves propagate and feed back on themselves leading to a self-excited unstable mode.

To apply the theory, both (7.3) and (7.4) must be integrated along the closed orbits existing inside the cavity. Since the base flow is steady and the streamlines are closed, (7.3) is a linear ODE with periodic coefficients whose general solution can be written in terms of Floquet modes. In particular, the solution can be found by building the fundamental Floquet matrix $\boldsymbol{M}(T)$, solution of the system

$$\frac{\mathrm{D}\boldsymbol{M}}{\mathrm{D}t} = -\boldsymbol{L}^t(\boldsymbol{X})\boldsymbol{M} \quad \text{with } \boldsymbol{M}(0) = \boldsymbol{I}, \tag{7.6}$$

and extracting its eigenvalues and the corresponding eigenvectors. Using these eigenvectors as initial conditions, it is possible to retrieve the temporal evolution of $\boldsymbol{k}$ during a lap around the closed streamline. Equation (7.3) admits three independent solutions related to the three eigenvectors of the fundamental Floquet matrix $\boldsymbol{M}(T)$. However, since the base flow is two-dimensional, there exists for each orbit one eigenvalue equal to one, with the corresponding eigenvector remaining constant in time and orthogonal to the base flow. In other words, since the third column of $\boldsymbol{L}$ and the third line of $\boldsymbol{L}^t$ are zero, the transverse component of $\boldsymbol{k}$ remains constant as time evolves. In contrast, the in-plane components evolve under the action of the deformation tensor. Once (7.3) is solved, the amplitude $\boldsymbol{a}$ can be found by integrating

(7.4). One can use any linear combination of the Floquet modes from (7.6) to set the specific $\boldsymbol{k}$ in (7.4).

Since we are trying to determine a self-excited mode, we need only to consider solutions of (7.3) that are periodic in time, i.e. solutions such that $\boldsymbol{k}(0) = \boldsymbol{k}(T)$. Moreover Bayly (1988), Lifschitz & Hameiri (1991) and Sipp & Jacquin (2000) have shown that centrifugal and hyperbolic instabilities attain their maximum growth rate for modes characterized by purely transverse wavenumbers. Therefore, only eigenvectors orthogonal to the base flow will be considered in the following analysis. Solutions of (7.4) associated with a $\boldsymbol{k}$ orthogonal to the plane of motion are usually termed pressureless modes (see also Godeferd *et al.* 2001). With this choice, (7.4) reduces to an ordinary linear differential equation with periodic coefficients. According to Floquet theory, its solution can be written in terms of Floquet modes

$$\boldsymbol{a}(t) = \bar{\boldsymbol{a}}(t)\exp(\sigma t), \tag{7.7}$$

where $\bar{\boldsymbol{a}}(t)$ is a periodic function (with the same period T as the material point moving along the selected closed streamline) and $\mathrm{Re}\{\sigma\} = \sigma_r$ is the growth rate of the perturbation. In order to make a quantitative comparison with the eigenvalues predicted by the global analysis, we have to compute the values of σ in (7.7) for each closed orbit inside the cavity. To this end, we parameterize each streamline, and the corresponding growth rate σ, with the distance along the horizontal line connecting the centre of the vortex to the left-hand wall of the cavity (see figure 11).

As for (7.3), the fundamental Floquet matrix $\boldsymbol{A}$ corresponding to (7.4) is built by integrating the system

$$\frac{\mathrm{D}\boldsymbol{A}}{\mathrm{D}t} = \left(\frac{2\boldsymbol{k}\boldsymbol{k}^{\mathrm{T}}}{|\boldsymbol{k}|^2} - \boldsymbol{I}\right)\boldsymbol{L}(\boldsymbol{X})\boldsymbol{A}, \tag{7.8}$$

$$\boldsymbol{A}(0) = \boldsymbol{I}, \tag{7.9}$$

along each orbit. The eigenvalues $\mu_i(x_0)$ and the corresponding eigenvectors of $\boldsymbol{A}(T)$ are then easily extracted.

As mentioned above, since the base flow is two-dimensional and the wave-vector $\boldsymbol{k}$ is orthogonal to the x–y plane, we expect one eigenvalue of $\boldsymbol{A}$ to be 1. The other two, for the incompressibility constrain, must multiply to 1, i.e. $\mu_1(x_0)\ \mu_2(x_0) = 1$. The Floquet exponent $\sigma(x_0)$ of the perturbation on the selected orbit ψ_0 is obtained from the Floquet multiplier $\mu(x_0)$ of $\boldsymbol{A}$ by the simple relation

$$\sigma^{\{n\}}(\psi_0) = \sigma_r(\psi_0) + \mathrm{i}\sigma_i^{\{n\}}(\psi_0) = \frac{\log(\mu)}{T(\psi_0)} + \mathrm{i}\frac{2n\pi}{T(\psi_0)} \quad \text{with } n \in \mathbb{N}, \tag{7.10}$$

where $T(\psi_0)$ is the period of revolution.

The growth rate of each WKBJ mode is simply given by the real part of $\sigma^{\{n\}}$. The frequency is related to the imaginary part and is not unique. According to the formula (7.10), modes with the same growth rate (at leading order) but different frequencies are admissible: in particular the admissible frequencies are integer multiple of the frequency of revolution along the same streamline.

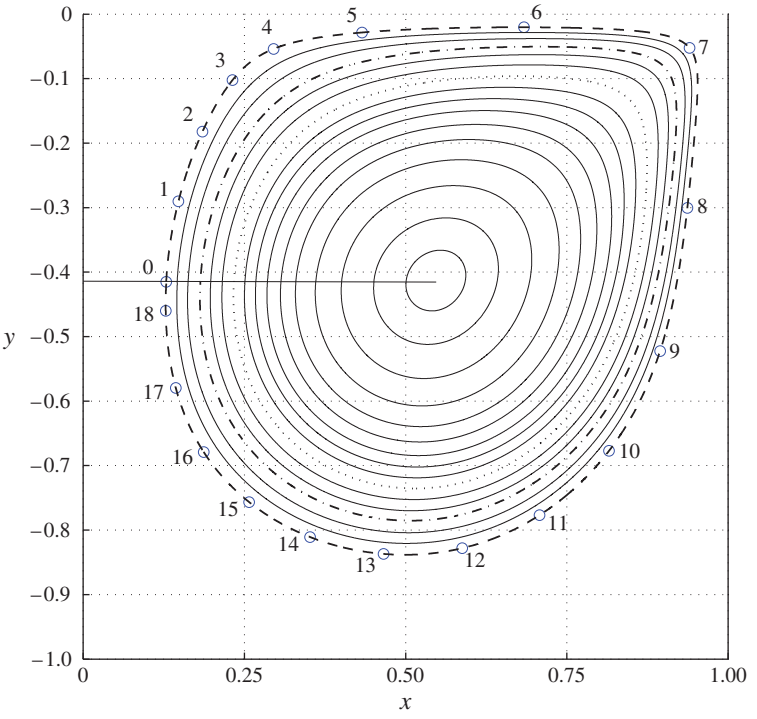

FIGURE 11. (Colour online) Streamlines for the flow inside the cavity at $Re = 1370$. The asymptotic inviscid stability theory identifies three streamlines along which three different WKBJ modes present their maximum growth rate: - - - -, orbit of the global maximum growth rate pertaining to the steady mode σ_∞ (see figure 12); — · —, orbit of the unsteady mode related to σ_2; · · · · · ·, orbit of the steady mode related to σ_3. The evolution of a particle along the streamline - - - - is also depicted. The revolution period of this streamline is $T = 18.3$. The horizontal line connecting the centre of the vortex to the left-hand wall of the cavity is used in the present work to parameterize the streamlines.

7.1. *Asymptotic estimate of the first bifurcation*

The numerical computations of the asymptotic stability are performed on the same base flow fields as used for the global stability analysis. Several numerical methods are available to solve the system of ODEs (7.5)–(7.8) along with their initial conditions. We chose a fourth-order Runge–Kutta method: starting from the points located on the horizontal line, connecting the centre of the vortex to the left-hand wall of the cavity (see figure 11), the algorithm marches along the orbits ensuring the spatial periodicity of each streamline. In the figure we also report the position of a material point along its trajectory at equal time intervals to give a visual impression of the local velocity along the streamline.

The asymptotic eigenpairs have been computed with several discretizations and only the eigenvalues with an accuracy of four significant digits are presented. In figure 12, we show the real and imaginary part of the eigenvalues obtained with the WKBJ approximation as function of the x coordinate defining the different orbits.

The asymptotic analysis reveals three maxima of the growth rates $\sigma_{r\infty}(=\sigma_{r1})$, which is also the global maximum, σ_{r2} and σ_{r3}. The first and the third branches (σ_1 and σ_3) are characterized by zero-frequency eigenvalues, while the second branch

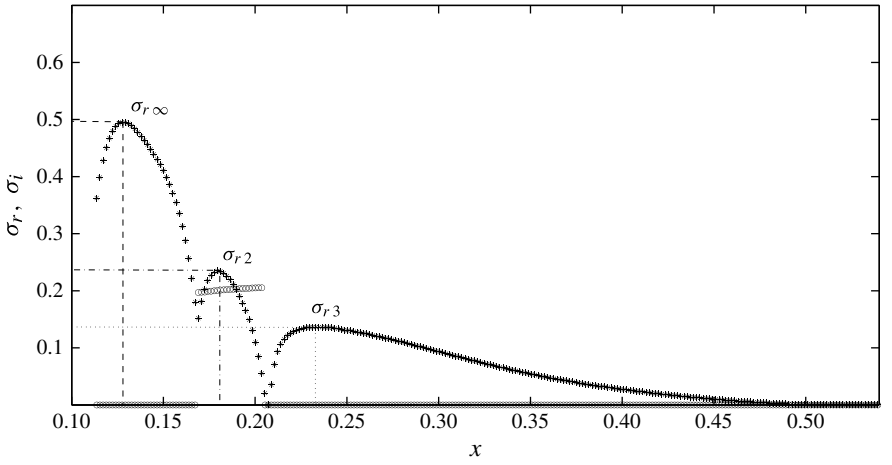

FIGURE 12. WKBJ growth rate σ_r ($*$) and eigenfrequency σ_i ($\bigcirc$) at $Re_{BF} = 1370$. Here the parameter x is the physical coordinate showed in figure 11. The lines denote the maximum of the different branches: ----, maximum inviscid growth rate $\sigma_{r\infty}$; — · —, maximum related to second branch σ_{r2}; · · · · · ·, third maximum σ_{r3}.

(σ_2) is associated with unstable oscillations with frequency of $\approx$0.2. As further discussed below, the closed streamline of maximum growth rate $\sigma_{r\infty}$ is located within the wavemaker of stationary unstable global mode.

However, despite this agreement, the viscous correction term and the correction term relative to finite wavenumber effects need to be taken into account for a correct prediction of the instability, see Landman & Saffman (1987) and Gallaire *et al.* (2007).

In figure 13(a) we report the growth rate of the unstable mode computed on the base flow at $Re_{BF} = 1370$ when increasing the Reynolds number in the linearized stability equations, Re_{STB}, and the growth rate obtained by integrating along the closed orbits with the corrections discussed in appendix A,

$$s = \sigma(\psi_0) - \frac{A}{k} - \frac{k^2}{Re_{BF}}. \tag{7.11}$$

The value of A above is not estimated by a least square fitting as in previous studies, but computed analytically using the information provided by the local adjoint and direct field on the streamline. The values obtained with this procedure are reported in table 2. Figure 13(a) shows that the scaling provided by the global stability analysis estimates correctly the asymptotic growth rate $\sigma_{r\infty}$. The corresponding optimal spanwise wavenumber k is depicted in 13(b) as a function of $Re_{STB}^{1/3}$. The spanwise wavenumber, like the maximal growth rate, follows the correct scaling laws, $\sigma_r \propto Re_{STB}^{-1/3}$ and $k_{opt} \propto Re_{STB}^{1/3}$ (Bayly 1988; Sipp *et al.* 1999).

Finally, we focus our attention on the spatial distribution of the structural sensitivity fields computed with the maximum Re_{STB} considered (equal to 300 000). Figure 14(a) shows the agreement between the critical streamline (i.e. the streamline ψ where the inviscid growth rate is maximum) and the sensitivity map. At large (stability) Reynolds numbers Re_{STB}, therefore, the sensitivity analysis indicates that the instability core is located on the orbit with maximum growth rate.

The global analysis performed at Re_{BF} also provides information about the sub-critical branches arising in the asymptotic computations. We depict the structural

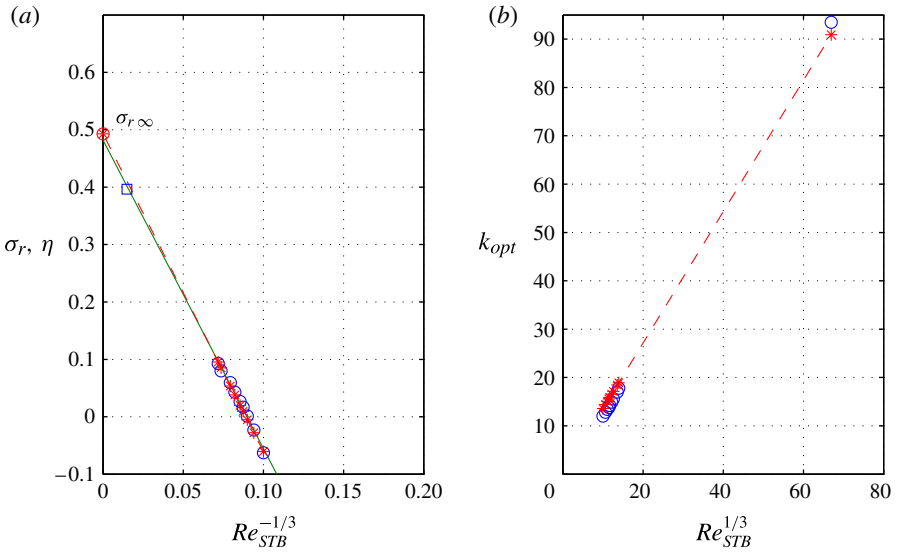

FIGURE 13. (Colour online) Global and asymptotic stability results. (*a*) Viscous growth rate η (○, □ $= Re_{STB} = 300\,000$) at $Re_{BF} = 1370$ and asymptotic estimate of growth rate σ_r (∗- - - -) according to the correction in appendix A. We also depict the regression line (——) related to the global growth rates. (*b*) Optimal global spanwise wavenumber k_{opt} (○) and prediction from the asymptotic theory (∗) as a function of $Re_{STB}^{1/3}$. The predicted optimal spanwise wavenumber is simply obtained by finding the maximum of the scaling law (A 6), i.e. $k = (Re_{STB}A/2)^{1/3}$.

Δt_{orbit}	k	$\mathscr{J}$	A
0.0050	13.4	0.00637	5.1143
0.0025	13.4	0.00678	5.0148
0.0010	13.4	0.00681	5.0078

TABLE 2. Convergence of parameters arising in the asymptotic estimation (see appendix A) of the viscous growth rate; Δt_{orbit} is the step used to discretize the critical orbit. (Here, $Re_{BF} = 1370$).

sensitivity extracted from the global analysis of these two sub-critical WKBJ eigenmodes in figure 14(*b*,*c*). As for the leading eigemode we observe an excellent correspondence between the sensitivity spatial map and the two critical orbits. Interestingly, we note also the agreement between the frequency of mode σ_2 (see figure 14*b*) and the frequency predicted by the WKBJ analysis. From a physical point of view, this matching can be associated with the fact that these eigenmodes are of centrifugal nature, i.e. inviscid, and therefore the inviscid structural sensitivity is able to isolate accurately the regions where each of the three instability branches presents the main contribution to the instability mechanism.

7.2. *Asymptotic results for* $Re_{BF} = 4140$

As previously discussed, when we consider the stability to three-dimensional perturbations at supercritical Reynolds numbers, we find several unstable branches

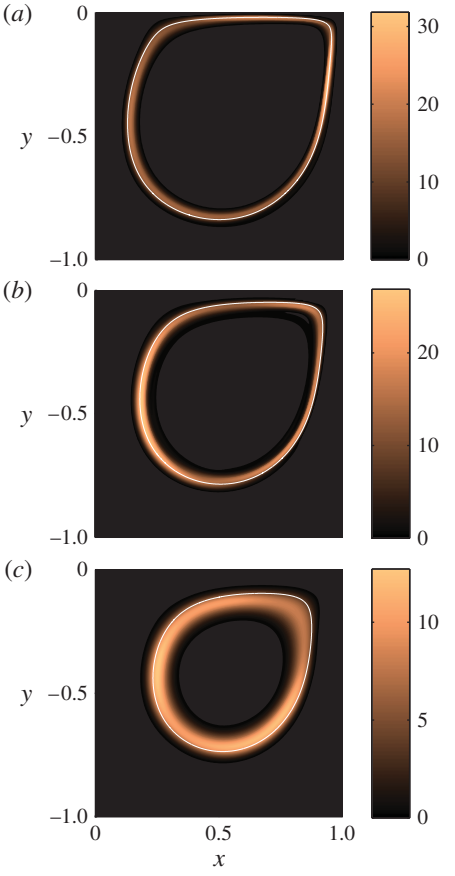

FIGURE 14. (Colour online) Comparison between the optimal streamline of WKBJ branches and sensitivity maps related to (global) eigenvalues: (*a*) $0.36 + \mathrm{i}0.00$; (*b*) $0.14 + \mathrm{i}0.20$; (*c*) $0.07 + \mathrm{i}0.00$. Parameter settings: $Re_{BF} = 1370$, $Re_{STB} = 300\,000$ and $k = 93.5$.

(see figure 3). If we consider the spanwise wavenumber $k = 22$ and $Re_{BF} = 4140$, we observe the occurrence of several harmonics of the fundamental leading eigenvalue. As shown in figure 3(*b*), these modes are characterized by a quantized eigenfrequency, $\omega \approx 0.32n$ with n integer. To show that the asymptotic analysis is also able to accurately predict the frequency of these harmonics, we carry out computations for the base flow at Reynolds number $Re_{BF} = 4140$ and report the results in figure 15, using the same conventions used for the onset of the bifurcation, for $Re_{BF} = 1370$, in figure 12. We first need to identify the closed streamlines and then calculate the instability properties along the orbit. We observe again three local maxima of the asymptotic growth rate, corresponding to two steady and one time-dependent modes.

The variation of the revolution period T as a function of the coordinate x, defining the different orbits, is depicted in the upper half of figure 16, while the corresponding orbits inside the cavity are displayed in the lower half. The main result we present here is that the period of the higher harmonics of the zero-frequency leading mode is selected by the period of revolution along the streamline of maximum growth rate. In table 3 we show that the frequencies obtained from the global stability analysis and

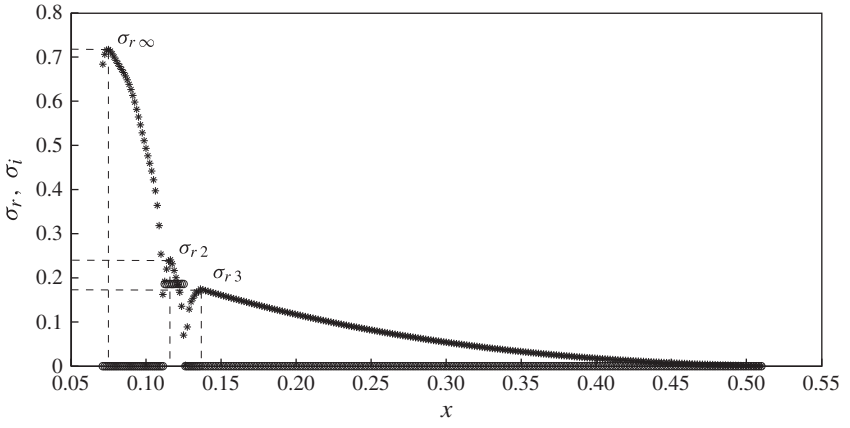

FIGURE 15. Asymptotic results for $Re_{BF} = 4140$. See figure 12 for details.

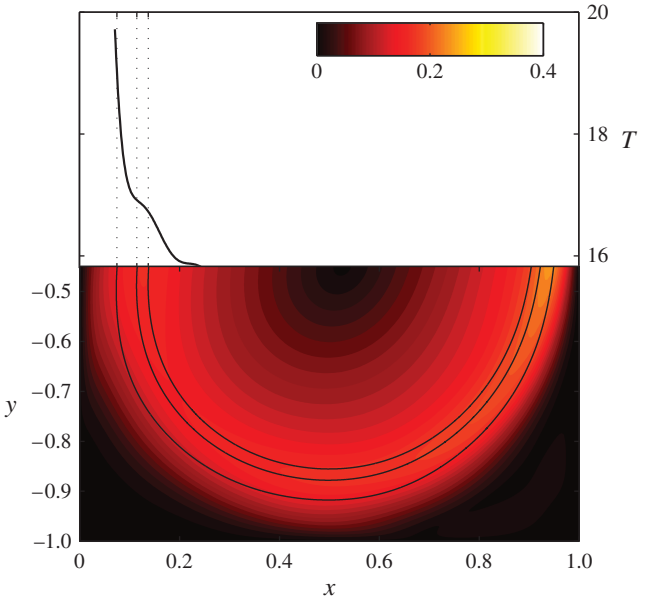

FIGURE 16. (Colour online) Revolution period of cavity orbits as a function of the abscissa x (upper half). Contour plot of the base flow modulus ($\|\boldsymbol{u}_b\|_2$) at $Re_{BF} = 4140$ and the three streamlines corresponding to the local maxima of the inviscid growth rate in figure 15 (lower half).

displayed in figure 3 do indeed correspond to the frequency computed by the local analysis (7.10). It is interesting to note that the global mode frequencies are uniquely related to the revolution period of a Lagrangian particle transported along the orbit. Thus, we conclude that the different frequencies of the multiple unstable branches are obtained as multiples n of the period of revolution along the critical (most unstable) orbit; the data in the table show an error lower than 5 %.

Harmonic n	Global mode frequency ω	Orbit period T	WKBJ frequency $\sigma_i^{\{n\}}(\psi_0) = 2n\pi/T$	Percentage error (%)
0	0.000	19.5	0.00	—
1	0.302	19.5	0.32	4.2
2	0.610	19.5	0.64	4.7
3	0.920	19.5	0.96	4.5

TABLE 3. Comparison of the results obtained using global stability analysis with those provided by the asymptotic analysis. We selected the orbit that has the maximum inviscid growth rate using a base flow characterized by $Re_{BF} = 4140$. The WKBJ frequencies are calculated according to (7.10).

8. Final remarks

In this work, we study the instability of the flow past an infinitely wide open square cavity. First, we identify the critical Reynolds number ($Re_{BF} = 1370$) at which the first bifurcation occurs. This instability drives the flow from a steady two-dimensional to a steady three-dimensional configuration characterized by a relatively short modulation in the spanwise direction, the spanwise scale of the modulation being of about 0.47 cavity depths.

The spatial structure of the direct and adjoint eigenmodes is examined to describe the features of the flow past the bifurcation. The direct mode is concentrated inside the cavity in a circular region with a tail on the shear region just above the downstream wall; the adjoint mode has a similar structure except for a small region near the upstream edge of the cavity where the flow is most receptive to momentum forcing. The overlapping of these two fields provides information about the instability mechanism (the so-called wavemaker) and is concentrated within the square cavity, suggesting that the generation of the instability mechanism is spatially concentrated around a closed streamline inside the cavity, around the core vortex.

We examine different types of cavity flows (i.e. characterized by different boundary conditions) and identify the corresponding critical Reynolds number at which the first bifurcation occurs. As proposed by Brés & Colonius (2008), we confirm that the mean velocity computed along the line connecting the two opposite edges allows us to roughly estimate the critical conditions at which the first bifurcation arises. The critical value of a Reynolds number based on this averaged velocity, the cavity depth and the fluid viscosity is found to be $Re_{av} \approx 470$.

The sensitivity to base flow modifications is then considered to study the mechanisms that can suppress or enhance the instability. We follow here the approach by Meliga & Chomaz (2011) and compute the optimal linear velocity distribution at the walls and at the inlet of the computational domain able to stabilize the flow. The resulting blowing/suction profiles show that each modification (when possible) is aimed at decreasing the total momentum of the cavity core vortex (identified above as the core of the instability).

The WKBJ approximation is then introduced to predict the first instability and its characteristics as suggested by Bayly (1988). Considering the asymptotic stability along the closed streamlines inside the cavity, we find three different branches of unstable orbits (two stationary branches and an unsteady branch) and select the three critical orbits ψ whose corresponding growth rates are local maxima ($\sigma_{r\infty}$, σ_{r2}, σ_{r3}). The asymptotic values of the growth rate and of the spanwise wavenumber of the

unstable modes show very good agreement with the global stability analysis once the correction for finite Reynolds number and spanwise length scale are applied to the inviscid asymptotic result. The three critical orbits detected by the asymptotic analysis are also shown to overlap with the structural sensitivity map of unstable modes at low viscosities, large Re_{STB} (we refer to this field as inviscid structural sensitivity). This procedure allows us to identify the spatial region where the core of the inviscid mechanism of the instability is located.

To identify a frequency selection mechanism for the time-dependent sub-leading unstable global modes emerging at supercritical conditions, we consider the stability of the flow at $Re_{BF} = 4140$ where the global analysis shows the occurrence of four branches of unstable modes characterized by frequencies that are multiples of a fundamental value ω_0. We show that the value of ω_0 corresponds to the period of revolution of Lagrangian fluid particles along the closed orbit of largest growth rate in the asymptotic limit. We thus conclude that the asymptotic theory is able to predict accurately the global stability results, enabling us to estimate the critical conditions leading to the instability. Furthermore, the inviscid structural sensitivity, discussed here, is a general concept that can be used whenever the instability is of inviscid type.

Appendix A. Construction of pressureless modes

In what follows we briefly recall the theory related to the dynamics of asymptotic modes (Bayly 1988). First of all, we express the evolution of the perturbation using the normal-mode ansatz

$$[\boldsymbol{u}', P'] = [\hat{\boldsymbol{u}}, \hat{P}] \exp\{\mathrm{i}kz + st\}. \tag{A 1}$$

The main idea is to use the eigenpairs of the fundamental Floquet matrix $\boldsymbol{M}(T)$ to build a vector basis $\boldsymbol{f}_i$ for the representation of the modes along the orbit:

$$\hat{\boldsymbol{u}}(\boldsymbol{x}) = \sum_{i=1}^{3} \hat{u}_i(\boldsymbol{x}) \boldsymbol{f}_i(\boldsymbol{x}). \tag{A 2}$$

This basis diagonalizes the nonlinear operator $\boldsymbol{u}_b \cdot \nabla(\,) + (\,) \cdot \nabla \boldsymbol{u}_b$ and can be computed as $\boldsymbol{f}_i = \mathrm{e}^{-\sigma t} \boldsymbol{M}(t) \boldsymbol{e}_i$. Considering the limit of $\|\boldsymbol{k}\| \to \infty$, we re-scale the WKBJ eigenmode as

$$[\hat{\boldsymbol{u}}, \hat{\boldsymbol{v}}, \hat{\boldsymbol{w}}, \hat{\boldsymbol{p}}](\tilde{\Psi}) = [\hat{\boldsymbol{U}}, \hat{\boldsymbol{V}}/k, \hat{\boldsymbol{w}}/\sqrt{k}, \hat{\boldsymbol{p}}/k\sqrt{k}](\tilde{\Psi}), \tag{A 3}$$

where the new streamfunction $\tilde{\Psi} = \sqrt{k}(\psi - \psi_0)$ allows us to magnify the region near the critical orbit ψ_0. Introducing the scaling (A 3) into the LEes, we get the equation of a quantum harmonic oscillator (see e.g. Bender & Orszag 1978)

$$\hat{\boldsymbol{U}}''(\tilde{\Psi}) + \left[\frac{A}{\mathscr{J}(\psi_0)} - \lambda^2 \tilde{\Psi}^2 \right] \hat{\boldsymbol{U}} = 0, \tag{A 4}$$

with $\hat{\boldsymbol{U}}(\pm\infty) = 0$, $\lambda^2 = -\sigma''(\psi_0)/(2\mathscr{J})$ and

$$\mathscr{J} = \frac{1}{T(\psi_0)} \int_0^{T(\psi_0)} (\boldsymbol{f}_1^{\dagger} \cdot \nabla\psi) \left[\sigma(\psi_0) + \frac{\mathrm{d}}{\mathrm{d}t} \right] \{\boldsymbol{f}_1 \cdot \nabla\psi\} \mathrm{d}t. \tag{A 5}$$

In (A 4), the constant A is the parameter that governs the scaling of the eigenvalue s (i.e. $s = \sigma(\psi_0) - A/k$) and the adjoint vector $\boldsymbol{f}_i^\dagger$ is normalized as $\boldsymbol{f}_i^\dagger \cdot \boldsymbol{f}_j = \delta_{ij}$.

A better quantitative estimate of the viscous growth rate can be achieved using the viscous correction introduced by Landman & Saffman (1987) (see also Gallaire *et al.* 2007). The composite estimation thus reads

$$s = \sigma(\psi_0) - \frac{A}{k} - \frac{k^2}{Re_{BF}}. \tag{A 6}$$

REFERENCES

ALBENSOEDER, S. & KUHLMANN, H. C. 2006 Nonlinear three-dimensional flow in the lid-driven square cavity. *J. Fluid Mech.* **569**, 465–480.

ALBENSOEDER, S., KUHLMANN, H. C. & RATH, H. J. 2001 Three-dimensional centrifugal-flow instabilities in the lid-driven-cavity problem. *Phys. Fluids* **13**, 121–136.

AMESTOY, P. R., DUFF, I. S., KOSTER, J. & L'EXCELLENT, J.-Y. 2001 A fully asynchronous multifrontal solver using distributed dynamic scheduling. *SIAM J. Matrix Anal. Applics.* **23** (1), 15–41.

AMESTOY, P. R., GUERMOUCHE, A., L'EXCELLENT, J.-Y. & PRALET, S. 2006 Hybrid scheduling for the parallel solution of linear systems. *Parallel Comput.* **32** (2), 136–156.

ARNOLDI, W. E. 1951 The principle of minimized iteration in the solution of the matrix eigenproblem. *Q. Appl. Maths* **9**, 17–29.

BARBAGALLO, A., SIPP, D. & SCHMID, P. J. 2009 Closed-loop control of an open cavity flow using reduced-order models. *J. Fluid Mech.* **641**, 1–50.

BAYLY, B. J. 1988 Three-dimensional centrifugal-type instabilities in inviscid two-dimensional flows. *Phys. Fluids* **31**, 56–64.

BAYLY, B. J. 1989 Computations of broad-band instabilities in a class of closed-streamline flows. In *Mathematical Aspects of Vortex Dynamics* (ed. R. E. Caflisch), Society for Industrial and Applied Mathematics.

BENDER, C. M. & ORSZAG, S. A. 1978 *Advanced Mathematical Methods For Scientists and Engineers*. McGraw-Hill.

BOTTARO, A., CORBETT, P. & LUCHINI, P. 2003 The effect of base flow variation on flow stability. *J. Fluid Mech.* **476**, 293–302.

BRÉS, G. A. & COLONIUS, T. 2007*a* Direct numerical simulations of three-dimensional cavity flows. *AIAA Paper* 2007-3405.

BRÉS, G. A. & COLONIUS, T. 2007*b* Three-dimensional linear stability analysis of cavity flows. *AIAA Paper* 2007-1126.

BRÉS, G. A. & COLONIUS, T. 2008 Three-dimensional instabilities in compressible flow over open cavities. *J. Fluid Mech.* **599**, 309–339.

DI CICCA, G. M., MARTINEZ, M., HAIGERMOSER, C. & ONORATO, M. 2013 Three-dimensional flow features in a nominally two-dimensional rectangular cavity. *Phys. Fluids* **25**, 097101.

DING, Y. & KAWAHARA, M. 1998 Linear stability of incompressible flow using a mixed finite element method. *J. Comput. Phys.* **139**, 243–273.

FAURE, T. M., ADRIANOS, P., LUSSEYRAN, F. & PASTUR, L. 2007 Visualization of the flow inside an open cavity at medium range Reynolds numbers. *Exp. Fluids* **42**, 169–184.

FAURE, T. M., PASTUR, L., LUSSEYRAN, F., FRAIGNEAU, Y. & BISCH, D. 2009 Three-dimensional centrifugal instabilities development inside a parallelepipedic open cavity of various shape. *Exp. Fluids* **47**, 395–410.

GALLAIRE, F., MARQUILLIE, M. & EHRENSTEIN, U. 2007 Three-dimensional tranverse instabilities in detached boundary layers. *J. Fluid Mech.* **571**, 221–233.

GHARIB, M. & ROSHKO, A. 1987 The effect of flow oscillations on cavity drag. *J. Fluid Mech.* **177**, 501–530.

GIANNETTI, F. 2015 WKBJ analysis in the periodic wake of a cylinder. *Theor. Appl. Mech. Lett.*; accepted for publication.

GIANNETTI, F. & LUCHINI, P. 2007 Structural sensitivity of the first instability of the cylinder wake. *J. Fluid Mech.* **581**, 167–197.

GIANNETTI, F., LUCHINI, P. & MARINO, L. 2010 Characterization of the three-dimensional instability in a lid-driven cavity by an adjoint based analysis. In *Seventh IUTAM Symposium on Laminar-Turbulent Transition* (ed. P. Schlatter & D. S. Henningson), IUTAM Bookseries, vol. 18, pp. 165–170. Springer.

GODEFERD, F. S., CAMBON, C. & LEBLANC, S. 2001 Zonal approach to centrifugal, elliptic and hyperbolic instabilities in Stuart vortices with external rotation. *J. Fluid Mech.* **449**, 1–37.

GONZALEZ, L. M., AHMED, M., KÜHNEN, J., KUHLMANN, H. C. & THEOFILIS, V. 2011 Three-dimensional flow instability in a lid-driven isosceles triangular cavity. *J. Fluid Mech.* **675**, 369–396.

GUERMOND, J. L., MIGEON, C., PINEAU, G. & QUARTAPELLE, L. 2002 Start-up flows in a three-dimensional rectangular driven cavity of aspect ratio 1:1:2 at $Re = 1000$. *J. Fluid Mech.* **450**, 169–199.

HAQUE, S., LASHGARI, I., GIANNETTI, F. & BRANDT, L. 2012 Stability of fluids with shear-dependent viscosity in the lid-driven cavity. *J. Non-Newtonian Fluid Mech.* **173–174**, 49–61.

HECHT, F. 2012 New development in freefem++. *J. Numer. Maths* **20**, 251–265.

LANDMAN, M. J. & SAFFMAN, P. 1987 The three-dimensional instability of strained vortices in a viscous fluid. *Phys. Fluids* **30**, 2339–2342.

LASAGNA, D., DONELLI, R., GREGORIO, F. D. & IUSO, G. 2011 Effect of a trapped vortex cell on a thick wing airfoil. *Exp. Fluids* **51**, 1369–1384.

LEHOUCQ, R., MASCHHOFF, K., SORENSEN, D. & YANG, C. 2007 Arpack software. website: http://www.caam.rice.edu/software/arpack/.

LIFSCHITZ, A. 1994 On the instability of certain motions of an ideal incompressible fluid. *Adv. Appl. Maths* **15**, 404–436.

LIFSCHITZ, A. & HAMEIRI, E. 1991 Local stability conditions in fluid dynamics. *Phys. Fluids* A **3**, 2644–2651.

LUCHINI, P. & BOTTARO, A. 2014 Adjoint equations in stability analysis. *Annu. Rev. Fluid Mech.* **46** (1), 493–517.

MARQUET, O., SIPP, D. & JACQUIN, L. 2008 Sensitivity analysis and passive control of cylinder flow. *J. Fluid Mech.* **615**, 221–252.

MAULL, D. J. & EAST, L. F. 1963 Three-dimensional flow in cavities. *J. Fluid Mech.* **16**, 620–632.

MELIGA, P. & CHOMAZ, J. M. 2011 Global modes in a confined impinging jet: application to heat transfer and control. *Theor. Comput. Fluid Dyn.* **25**, 179–193.

MESEGUER-GARRIDO, F., DE VICENTE, J., VALERO, E. & THEOFILIS, V. 2014 On linear instability mechanism in incompressible open cavity flow. *J. Fluid Mech.* **752**, 219–236.

MIGEON, C., PINEAU, G. & TEXIER, A. 2003 Three-dimensionality development inside standard parallelepipedic lid-driven cavities at $Re = 1000$. *J. Fluids Struct.* **17**, 717–738.

MIGEON, C., TEXIER, A. & PINEAU, G. 2000 Effects of lid-driven cavity shape on the flow establishment phase. *J. Fluids Struct.* **14**, 469–488.

PRALITS, J. O., BRANDT, L. & GIANNETTI, F. 2010 Instability and sensitivity of the flow around a rotating circular cylinder. *J. Fluid Mech.* **650**, 513–536.

ROCKWELL, D. & KNISELY, C. 1980 Observations of the three-dimensional nature of unstable flow past a cavity. *Phys. Fluids* **23**, 425–431.

ROCKWELL, D. & NAUDASCHER, E. 1978 Review – self-sustaining oscillations of flow past cavities. *Trans. ASME: J. Fluids Engng* **100**, 152–165.

ROSSITER, J. E. 1964 Wind-tunnel experiments on the flow over rectangular cavities at subsonic and transonic speeds. *Tech. Rep.* 3438, http://naca.central.cranfield.ac.uk/reports/arc/rm/3438.pdf.

ROWLEY, C. W., COLONIUS, T. & BASU, A. J. 2002 On self-sustained oscillations in two-dimensional compressible flow over rectangular cavities. *J. Fluid Mech.* **455**, 315–346.

SHATROV, V., MUTSCHKE, G. & GERBETH, G. 2003 Three-dimensional linear stability analysis of lid-driven MHD cavity flow. *Phys. Fluids* **15**, 2141–2151.

SIPP, D. 2012 Open-loop control of cavity oscillations with harmonic forcings. *J. Fluid Mech.* **708**, 439–468.

SIPP, D. & JACQUIN, L. 2000 Three-dimensional centrifugal-type instabilities of two-dimensional flows in rotating systems. *Phys. Fluids* **12**, 1740–1748.

SIPP, D., LAUGA, E. & JACQUIN, L. 1999 Vortices in rotating systems: centrifugal, elliptic and hyperbolic type instabilities. *Phys. Fluids* **11**, 3716–3728.

SIPP, D. & LEBEDEV, A. 2007 Global stability of base and mean flows: a general approach and its applications to cylinder and open cavity flows. *J. Fluid Mech.* **593**, 333–358.

THEOFILIS, V. 2000 Globally unstable basic flows in open cavities. *AIAA Paper* 00-1965.

DE VICENTE, J., BASLEY, J., MESEGUER-GARRIDO, F., SORIA, J. & THEOFILIS, V. 2014 Three-dimensional instabilities over a rectangular open cavity: from linear stability analysis to experimentation. *J. Fluid Mech.* **748**, 189–220.

DE VICENTE, J., RODRIGUEZ, D., THEOFILIS, V. & VALERO, E. 2010 Stability analysis in spanwise-periodic double-sided lid-driven cavity flows with complex cross-sectional profiles. *Comput. Fluids* **43**, 143–153.

YAMOUNI, S., SIPP, D. & JACQUIN, L. 2013 Interaction between feedback aeroacoustic and acoustic resonance mechanisms in a cavity flow: a global stability analysis. *J. Fluid Mech.* **717**, 134–165.

ZHANG, K. & NAGUIB, A. M. 2006 Dispersion relation and mode selectivity in low-Mach-number cavity flows. *AIAA Paper* 2006-3229.

ZHANG, K. & NAGUIB, A. M. 2008 Effect of cavity width on the unsteady pressure in a low-Mach-number cavity. *AIAA J.* **46**, 1878–1880.

ZHANG, K. & NAGUIB, A. M. 2011 Effect of finite cavity width on flow oscillation in a low-Mach-number cavity flow. *Exp. Fluids* **51**, 1209–1229.